

See discussions, stats, and author profiles for this publication at: <https://www.researchgate.net/publication/263510413>

# ChemInform Abstract: Local Structure and Dynamics in the Na Ion Battery Positive Electrode Material $\text{Na}_3\text{V}_2(\text{PO}_4)_2\text{F}_3$ .

ARTICLE in CHEMINFORM · JULY 2014

Impact Factor: 0.74 · DOI: 10.1002/chin.201428013

---

READS

75

9 AUTHORS, INCLUDING:



Zigeng Liu

University of Cambridge

6 PUBLICATIONS 98 CITATIONS

SEE PROFILE



Matthew Dunstan

University of Cambridge

23 PUBLICATIONS 201 CITATIONS

SEE PROFILE



Guiming Zhong

Xiamen University

20 PUBLICATIONS 106 CITATIONS

SEE PROFILE



Yong Yang

Xiamen University

187 PUBLICATIONS 3,314 CITATIONS

SEE PROFILE

# Local Structure and Dynamics in the Na Ion Battery Positive Electrode Material $\text{Na}_3\text{V}_2(\text{PO}_4)_2\text{F}_3$

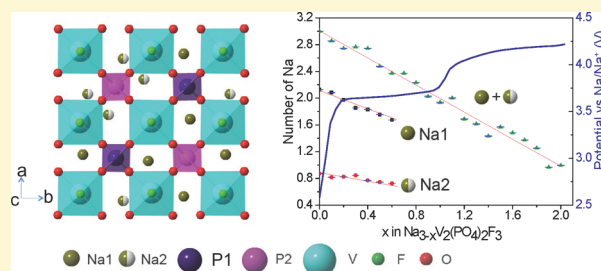
Zigeng Liu,<sup>†,‡</sup> Yan-Yan Hu,<sup>‡</sup> Matthew T. Dunstan,<sup>‡</sup> Hua Huo,<sup>‡</sup> Xiaogang Hao,<sup>†</sup> Huan Zou,<sup>†</sup> Guiming Zhong,<sup>†</sup> Yong Yang,<sup>\*,†</sup> and Clare P. Grey<sup>\*,‡</sup>

<sup>†</sup>State Key Lab for Physical Chemistry of Solid Surface and Department of Chemistry, College of Chemistry and Chemical Engineering, Xiamen University, Xiamen 361005, Fujian, China

<sup>‡</sup>Chemistry Department, University of Cambridge, Lensfield Rd, Cambridge CB2 1EW, U.K.

## S Supporting Information

**ABSTRACT:**  $\text{Na}_3\text{V}_2(\text{PO}_4)_2\text{F}_3$  is a novel electrode material that can be used in both Li ion and Na ion batteries (LIBs and NIBs). The long- and short-range structural changes and ionic and electronic mobility of  $\text{Na}_3\text{V}_2(\text{PO}_4)_2\text{F}_3$  as a positive electrode in a NIB have been investigated with electrochemical analysis, X-ray diffraction (XRD), and high-resolution  $^{23}\text{Na}$  and  $^{31}\text{P}$  solid-state nuclear magnetic resonance (NMR). The  $^{23}\text{Na}$  NMR spectra and XRD refinements show that the Na ions are removed non-selectively from the two distinct Na sites, the fully occupied Na1 site and the partially occupied Na2 site, at least at the beginning of charge. Anisotropic changes in lattice parameters of the cycled  $\text{Na}_3\text{V}_2(\text{PO}_4)_2\text{F}_3$  electrode upon charge have been observed, where  $a$  ( $= b$ ) continues to increase and  $c$  decreases, indicative of solid-solution processes. A noticeable decrease in the cell volume between 0.6 Na and 1 Na is observed along with a discontinuity in the  $^{23}\text{Na}$  hyperfine shift between 0.9 and 1.0 Na extraction, which we suggest is due to a rearrangement of unpaired electrons within the vanadium  $t_{2g}$  orbitals. The Na ion mobility increases steadily on charging as more Na vacancies are formed, and coalescence of the resonances from the two Na sites is observed when 0.9 Na is removed, indicating a Na1–Na2 hopping (two-site exchange) rate of  $\geq 4.6$  kHz. This rapid Na motion must in part be responsible for the good rate performance of this electrode material. The  $^{31}\text{P}$  NMR spectra are complex, the shifts of the two crystallographically distinct sites being sensitive to both local Na cation ordering on the Na2 site in the as-synthesized material, the presence of oxidized ( $\text{V}^{4+}$ ) defects in the structure, and the changes of cation and electronic mobility on Na extraction. This study shows how NMR spectroscopy complemented by XRD can be used to provide insight into the mechanism of Na extraction from  $\text{Na}_3\text{V}_2(\text{PO}_4)_2\text{F}_3$  when used in a NIB.



## ■ INTRODUCTION

Despite the popularity of Li ion batteries (LIBs) in energy storage applications, their relatively high cost and the geographic constraints associated with lithium resources have motivated a search for cheaper and more sustainable alternatives.<sup>1</sup> The lower cost and high abundance of Na make sodium ion batteries (NIBs) appealing alternatives.<sup>2–6</sup> The fundamental principles of NIBs and LIBs are similar, and many structurally related compounds may be used for both battery systems.

In recent years, due to their high operating voltage, capacity and stability, and low cost, fluoropolyanion-based active materials, such as  $\text{LiVPO}_4\text{F}$ ,  $\text{NaVPO}_4\text{F}$ , and  $\text{Na}_3\text{V}_2(\text{PO}_4)_2\text{F}_3$ ,<sup>7–9</sup> have attracted significant interest as alternatives to traditional metal oxides for use in both LIBs and NIBs.  $\text{Na}_3\text{V}_2(\text{PO}_4)_2\text{F}_3$ , in particular, due to its open NASICON framework and thermal stability, has shown excellent electrochemical performance as a cathode material in both LIBs and NIBs, giving rise to a highly reversible specific capacity (120 mAh/g) at a high average discharge voltage of 4.1 V vs  $\text{Li}^+/\text{Li}$  (3.8 V vs  $\text{Na}^+/\text{Na}$ ).<sup>10–15</sup>

The crystal structure of pristine  $\text{Na}_3\text{V}_2(\text{PO}_4)_2\text{F}_3$  has been studied by X-ray and neutron diffraction techniques<sup>8,16</sup> and modeled with first principles calculations.<sup>16</sup> The structure (Figure 1) exhibits  $P4_2/mnm$  symmetry and is composed of pairs of corner shared (via one F atom)  $\text{VO}_4\text{F}_2$  octahedra; these  $\text{VO}_4\text{F}_2$  octahedra are then equatorially connected to the  $\text{PO}_4$  tetrahedra via O atoms. Na ions are located in the open tunnel sites along the  $a$ - and  $b$ -axes (Figure 1a and b); this open NASICON type framework provides convenient diffusion pathways for Na ions. There are two different Na sites with an occupancy ratio of 2:1, and both are surrounded by four O ions and three F ions. The fully occupied Na site is denoted as Na1, with Na ions being slightly off center due to the repulsions between two neighboring Na1 ions. The other Na site (denoted as Na2) is partially occupied due to the short distance (1.87 Å) between two nearby Na2 sites. This partial occupancy leads to structural disorder, which will affect the

Received: November 10, 2013

Revised: March 20, 2014

Published: March 24, 2014

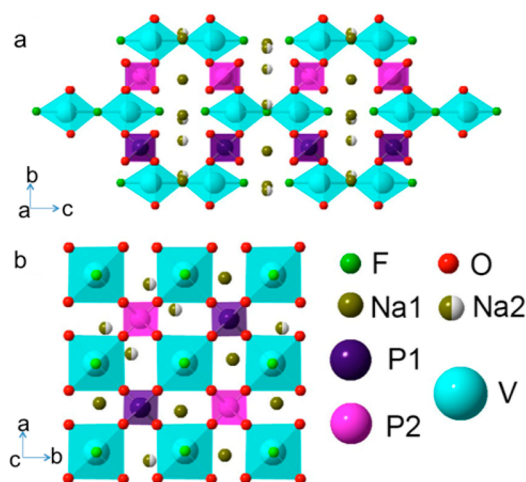


**Figure 1.** Schematic of the  $\text{Na}_3\text{V}_2(\text{PO}_4)_2\text{F}_3$  structure projected along the (a)  $a$ -axis and (b)  $c$ -axis. Na1 are fully occupied Na sites, while Na2 are half-occupied Na sites.<sup>8,16</sup>

local environments of the  $\text{PO}_4$  ions<sup>17,18</sup> (as will be explored in this paper).

The structural changes of the  $\text{Na}_3\text{V}_2(\text{PO}_4)_2\text{F}_3$  electrode during electrochemical cycling were previously investigated through X-ray diffraction and first principles calculations.<sup>15,16</sup> These studies provide valuable insight into correlations between the long-range bulk structural changes and the electrochemical properties. However, traditional diffraction techniques cannot directly probe local structural variations and dynamics, and uncertainty concerning the reaction mechanisms remains.

In this paper, we employ detailed *in* and *ex situ* X-ray diffraction and high-resolution  $^{23}\text{Na}$  and  $^{31}\text{P}$  solid-state nuclear magnetic resonance (ssNMR) experiments to follow both the long- and short-range structural and dynamical evolutions during battery charging. XRD provides information on long-range structural changes, whereas ssNMR is more suited to probe local structural environments, dynamics, and electronic structure. XRD reveals a solid solution process with only small structural changes of the NASICON framework upon  $\text{Na}^+$  extraction. Different Na and P sites can be distinguished via high-resolution  $^{23}\text{Na}$  and  $^{31}\text{P}$  ssNMR spectroscopy and relaxation time measurements, revealing the nonpreferential extraction of both Na1 and Na2 sites at least at the beginning of charge. Increasingly fast Na1–Na2 two-site exchange motion occurs as the number of Na vacancies increases, along with electronic structural changes within the  $\text{F}-\text{V}(\text{O}_4)\text{FV}(\text{O}_4)-\text{F}$  dimers that make up the NASICON framework. The results provide insight into the changes in the electrochemical profile of the  $\text{Na}_3\text{V}_2(\text{PO}_4)_2\text{F}_3$  electrode and its good electrochemical performance.

## EXPERIMENTAL SECTION

**Material Synthesis.** The  $\text{Na}_3\text{V}_2(\text{PO}_4)_2\text{F}_3/\text{C}$  composite was prepared using a two-step reaction process. The first step involves the synthesis of  $\text{VPO}_4/\text{C}$  powder from a mixture of  $\text{V}_2\text{O}_5$ ,  $\text{H}_3\text{PO}_4$ , and citric acid (molar ratio 1:2:2) dissolved in deionized water. The solution was continuously stirred at 80 °C for 12 h and then dried at 120 °C for 4 h to obtain a uniform gel. The gel was dried and then ball-milled for 6 h, pressed into pellets, and then heated at 350 °C for 6 h and at 700 °C for another 6 h in an argon atmosphere. The key feature of this synthesis method is the use of citric acid as both a chelating species and a carbon source since it forms a network of

amorphous carbon that covers the surface of the material after high-temperature heat treatment. It can, therefore, inhibit grain growth and improve the electronic conductivity of the composite.  $\text{VPO}_4/\text{C}$  and NaF were then mixed in a stoichiometric ratio of 2:3 in the second step, pressing the mixture into pellets, heating it at 700 °C for 6 h in a flow of argon, and then cooling it down to room temperature. Elemental analysis was performed in our prior study of this material, synthesized using the same synthetic procedure as used here,<sup>12</sup> and showed that the carbon content in the final  $\text{Na}_3\text{V}_2(\text{PO}_4)_2\text{F}_3/\text{C}$  composite is 6 wt %.

**Battery Preparation.** The electrochemical properties of  $\text{Na}_3\text{V}_2(\text{PO}_4)_2\text{F}_3$  were examined by using 2032 coin-type batteries, in which the positive electrode consisted of 85 wt %  $\text{Na}_3\text{V}_2(\text{PO}_4)_2\text{F}_3/\text{C}$  composite, 8 wt % Super P carbon, and 7 wt % poly-(tetrafluoroethylene) (PTFE) binder. Sodium metal supported on a current collector was used as the negative electrode. The two electrodes were separated by a piece of glass fiber sheet immersed in 1 M  $\text{NaClO}_4$  in propylene carbonate (PC) solution. The batteries were assembled in an argon glovebox and then cycled on an Arbin system. In order to investigate the structural evolution of  $\text{Na}_3\text{V}_2(\text{PO}_4)_2\text{F}_3$  following battery cycling by XRD and NMR, batteries were cycled and stopped at different states of charge and disassembled immediately in an argon glovebox. The materials were washed with dimethyl carbonate (DMC) three times and dried under vacuum before the characterization.

A flexible polyester bag-cell battery was used for *in situ*  $^{23}\text{Na}$  NMR measurements using methodology modified from that described earlier for our Li NMR studies.<sup>19</sup> A piece of Al mesh was used as the current collector on the positive electrode ( $\text{Na}_3\text{V}_2(\text{PO}_4)_2\text{F}_3$ ) side, and a Cu mesh was used on the Na metal anode side. The bag-cell battery was hermetically sealed with an impulse heat sealer in an argon glovebox. The *in situ* battery cell was placed in the middle of the coil and aligned vertically relative to the external magnetic field  $B_0$ . It was cycled at a current rate of  $C/100$  between 2.5 and 4.5 V, using a Bio-Logic VSP system. A low-pass filter (50 MHz) was used to remove the high frequency noise generated from the battery cycler.

**Material Characterization.** *Galvanostatic Intermittent Titration Technique (GITT).* The experiment was carried out by cycling a  $\text{Na}_3\text{V}_2(\text{PO}_4)_2\text{F}_3/\text{Na}$  battery with a current rate of  $C/20$  for 30 min and a 5-h rest between steps. The composition-dependent Na chemical diffusion coefficient  $\bar{D}_i$  is determined by the following equation:<sup>20</sup>

$$\bar{D}_i = \frac{4}{\pi} \left( \frac{V_M}{SFz_i} \right)^2 \left[ I_0 \left( \frac{dE}{d\delta} \right) / \left( \frac{dE}{d\sqrt{t}} \right) \right]^2 \left( t < \frac{L^2}{D} \right) \quad (1)$$

Where:  $V_M$ : molar volume of the sample ( $\text{cm}^3\text{mol}^{-1}$ ).

$S$ : total contact area between the electrolyte and the electrode ( $\text{cm}^2$ ). In this study, the apparent surface area is used instead as an approximation, thus overestimation is expected in the calculated diffusion coefficient.

$F$ : Faraday's constant ( $\text{A s mol}^{-1}$ )

$z_i$ : charge of the Na ion ( $z_i = 1$ )

$I_0$ : applied constant electric current (A)

$dE/d\delta$ : steady-state voltage change against Na composition ( $\text{V mol}^{-1}$ )

$dE/d\sqrt{t}$ : transient voltage change against the square root of time during the period of the current flux ( $\text{V s}^{-1/2}$ )

**X-ray Diffraction (XRD).** Room-temperature *in situ* powder XRD data were collected on a Panalytical Empyrean diffractometer using Cu K $\alpha$  radiation. A modified Swagelok battery was used for the *in situ* XRD measurements. In order to allow the X-rays to penetrate the positive electrode, an Al-coated Be disk window was used. A piece of carbon-coated kapton film was employed as the current collector; this film also helped to protect the Be window from corrosion at high voltages. The electrochemical cycling current rate was  $C/50$ . Sequential Rietveld refinements were carried out using GSAS,<sup>21</sup> with the graphical interface EXPGUI<sup>22</sup> to extract the cell parameters. Rietveld refinements were performed starting with the pattern obtained at the start of charge. Parameters refined included lattice parameters, atomic positions, thermal displacement parameters (with

the exception of O, whose  $U_{\text{iso}}$  was fixed at 0.01), and Na site occupancies. Subsequent patterns were then refined in a similar fashion, except that all thermal parameters were kept fixed at their final values extracted from the initial refinement. The thermal parameters of Na1 and Na2 were constrained to be the same.

**Solid-State Nuclear Magnetic Resonance (NMR).** *Ex situ*  $^{23}\text{Na}$  MAS NMR spectra were acquired on a Bruker AVIII-700 spectrometer, at a  $^{23}\text{Na}$  Larmor frequency of 185.2 MHz. All experiments were carried out using a double-resonance 1.3 mm MAS probe, spinning at frequencies of up to 50 kHz with a Hahn-echo pulse sequence ( $90^\circ$  pulse- $\tau$ - $180^\circ$  pulse- $\tau$ -acq). The  $90^\circ$  pulse length for  $^{23}\text{Na}$  was 1.25  $\mu\text{s}$  and recycle delay was 20 ms. All of the  $^{23}\text{Na}$  shifts were referenced to 1 M NaCl (aq) (0 ppm).

The *in situ*  $^{23}\text{Na}$  NMR spectra were acquired on a Bruker AVIII-300 spectrometer ( $^{23}\text{Na}$  Larmor frequency, 79.4 MHz) with a Bruker X-single resonance static probe and a 10-mm (in diameter) solenoid coil. The spectra were recorded at 90-min intervals using a Hahn-echo pulse sequence. The  $90^\circ$  pulse length for  $^{23}\text{Na}$  was 2.1  $\mu\text{s}$ , and the recycle delay was 50 ms.

$^{31}\text{P}$  MAS NMR spectra were collected on a Bruker AVIII-200 spectrometer, at a  $^{31}\text{P}$  Larmor frequency of 81.0 MHz. All experiments were performed using a 1.8 mm MAS probe, spinning at a frequency of 40 kHz. Due to the large  $^{31}\text{P}$  spectral range and limited excitation bandwidth of the NMR radio frequency (rf) pulses, in order to extract quantitative spectra, the stepwise nuclear spin-echo Fourier-transform mapping method<sup>23</sup> was used with a step size of  $\gamma B_1$  (corresponding to the rf pulse power level). The  $90^\circ$  pulse length was 1.6  $\mu\text{s}$ , and the recycle delay was 50 ms. The  $^{31}\text{P}$  shifts were referenced to 85%  $\text{H}_3\text{PO}_4$  (aq) (0 ppm).

## RESULTS

**Electrochemistry.**  $\text{Na}_3\text{V}_2(\text{PO}_4)_2\text{F}_3$ , when used as a cathode in a NIB, shows excellent electrochemical performance. The voltage-composition (capacity) plot obtained with the GITT method is shown in Figure 2, and a reversible capacity of 128 mAh/g is achieved. The gradual increases in voltage from 3.6 to 3.7 V (Stage I) and from 4.05 to 4.5 V (Stage II and III) indicate that solid solution (or single-phase) processes are occurring, consistent with previous X-ray diffraction studies and calculations.<sup>16</sup> The sudden voltage increase at the end of Stage I, corresponding to the extraction of one Na/per formula unit (specific capacity of 64 mAh/g) has been attributed to extraction from Na2 vs Na1 sites during Stages I and II/III, respectively.<sup>16</sup> The slope in the voltage profile is noticeably smaller from 4.2 V until the end of charge, suggesting that the higher voltage ( $x = 1$ –2) process should be divided into two stages (II and III).

Na chemical diffusion coefficients were estimated from the voltage response to the small current pulses applied during the GITT experiment<sup>20</sup> (Figure 2b). The approach is valid so long as the system is in a single-phase (i.e., solid solution) regime. We were unable to analyze the region from  $x = 0$  to 0.2, due to the difficulty in achieving equilibrium in the GITT curve at the beginning of charge, possibly due to surface dominated processes. As seen in Figure 2b, the chemical diffusivity  $\tilde{D}_i$  of the Na ions beyond  $x = 0.2$  increases gradually in both stages, but with a different slope in Stage I vs Stage II; it then drops rapidly in Stage III.

Detailed XRD and solid-state NMR investigations were carried out in order to understand the reaction mechanisms in more detail and to correlate the electrochemical performance with the changes in long-/short-range structures and dynamics of the  $\text{Na}_3\text{V}_2(\text{PO}_4)_2\text{F}_3$  electrode.

**XRD.** The *in situ* XRD patterns collected during the first charge (in Figure 3a; representative full patterns shown in Supplementary Figure S1) can be divided into three stages,

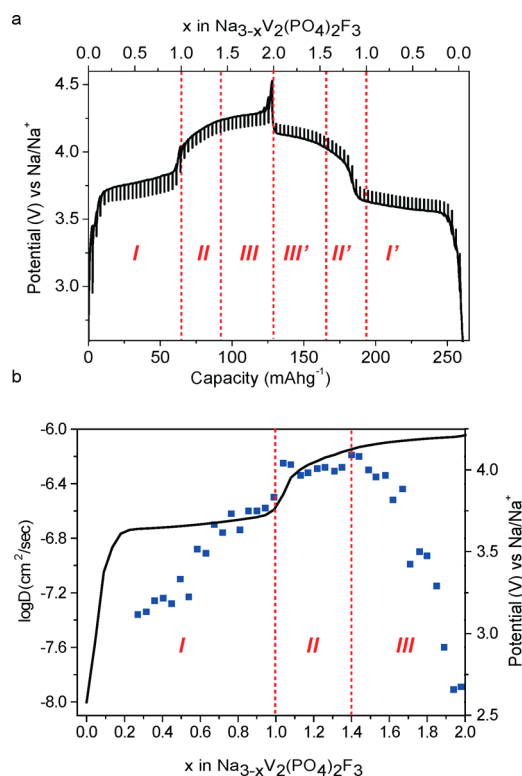


**Figure 2.** (a) Galvanostatic intermittent titration technique (GITT) plot, obtained by cycling a  $\text{Na}_3\text{V}_2(\text{PO}_4)_2\text{F}_3/\text{Na}$  battery with a constant current of 6.4 mA/g (corresponding to  $C/20$  with  $C = 128$  mAh/g) for 30 min with a 5-h rest between steps. (b) Variation of the  $\text{Na}^+$  chemical diffusion coefficient  $\tilde{D}_i$  over Stages I, II, and III (calculated with eq 1).

which are the same as those used in the analysis of the electrochemical profile (Figure 2). Careful examination of the  $\langle 220 \rangle$  reflection reveals only minimal changes at the early stage of charge ( $x = 0$ –0.4), and then the  $\langle 220 \rangle$  reflection gradually shifts to higher angles until the end of Stage I. In Stages II and III, this gradual shift continues with a slower rate as compared to that observed in Stage I.

Rietveld refinements using the full range of the XRD patterns (Supplementary Figure S1) were carried out, and the refined lattice parameters ( $a (= b)$  and  $c$ ), and unit cell volume  $V$  are shown in Figure 2b–d. The lattice parameter  $c$  exhibits a continuous increase over the full range of the charge process, suggesting solid-solution processes. The lattice changes are, however, anisotropic, the  $a (= b)$  parameter decreasing throughout the charge; a steeper decrease is observed between  $x = 0.4$ –1.0 compared with other states of charge. The trend of change in the unit cell volume mirrors that of the  $a$ -parameter.

**$^{23}\text{Na}$  NMR.** Figure 4 shows the complete series of (*ex situ*)  $^{23}\text{Na}$  NMR spectra from the cycled  $\text{Na}_3\text{V}_2(\text{PO}_4)_2\text{F}_3$  electrodes during the charge process. The  $^{23}\text{Na}$  NMR spectrum of pristine  $\text{Na}_3\text{V}_2(\text{PO}_4)_2\text{F}_3$  exhibits two major resonances at 92 and 146 ppm, respectively, with an intensity ratio of approximately 1:2, which are assigned to the partially filled Na2 site and the fully occupied Na1 site, respectively, according to the occupancy ratio ( $\text{Na2}:\text{Na1} = 1:2$ ) of the two Na sites in the crystal structure. The deviation of the resonance positions from the typical chemical shift range found in diamagnetic Na-containing compounds (close to 0 ppm) is due to the hyperfine interaction



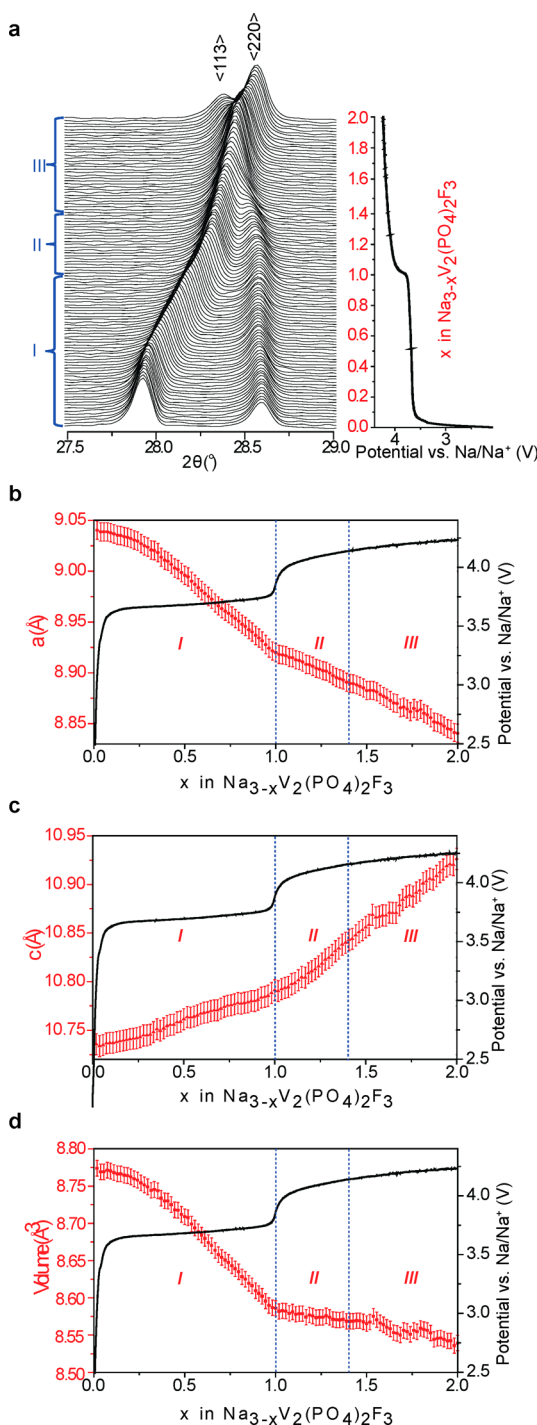


**Figure 3.** (a) *In situ* X-ray diffraction (XRD) patterns of the  $\text{Na}_3\text{V}_2(\text{PO}_4)_2\text{F}_3$  electrode (in the  $2\theta$  angle range of  $27.5^\circ$ – $29.0^\circ$ ) at different states of charge. (b,c) Variation of lattice parameters  $a$  ( $=b$ ) and  $c$ , respectively, and (d) the unit cell volume  $V$ , upon battery charging, derived from the Rietveld refinements performed using the *in situ* XRD patterns. Representative refinement patterns at  $x = 0$ , 1, and 2 are shown in Supplementary Figure S1, and relevant refinement statistics are listed in the Supporting Information.

and results from spin-density transfer from the paramagnetic  $\text{V}^{3+}$  ( $d^2$ ) ions to the Na  $s$ -orbitals.

Weaker peaks are observed below 50 ppm, likely from defective/oxidized sites, with mixed valency ( $\text{V}^{3+}/\text{V}^{4+}$ ) for vanadium. These are tentatively associated with O for F exchange in the  $\text{VO}_4\text{F}_2$  octahedra, as has been observed in prior

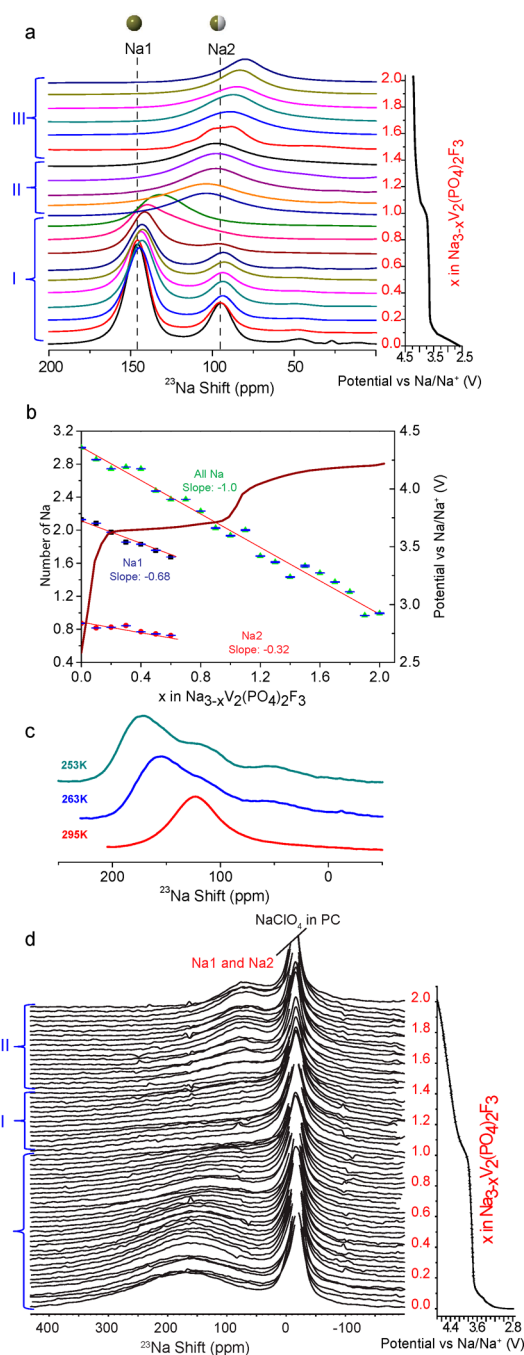


**Figure 4.** (a) *Ex situ*  $^{23}\text{Na}$  NMR spectra of  $\text{Na}_3\text{V}_2(\text{PO}_4)_2\text{F}_3$  electrodes at different states of charge. (b) Quantification of the Na1 sites (black filled squares), Na2 sites (red filled circles), and the total Na content (green filled triangles), following battery charging, performed by integrating each  $^{23}\text{Na}$  resonance. The extraction rates for the two Na sites and the total Na content, calculated from the slope of the quantification plots, are given. Error bars (of the size of symbols) are indicated. (c)  $^{23}\text{Na}$  spectra of  $\text{Na}_{3-x}\text{V}_2(\text{PO}_4)_2\text{F}_3$  at  $x = 1$ , collected at three different temperatures from 295 to 253 K. (d) *In situ*  $^{23}\text{Na}$  NMR spectra ( $-150$  ppm to  $430$  ppm) obtained from a  $\text{Na}_3\text{V}_2(\text{PO}_4)_2\text{F}_3/\text{Na}$  bag-cell battery cycled at a current rate of  $C/100$  over the voltage window of 2.5 to 4.5 V. The electrolyte peak ( $<0$  ppm) is truncated in order to show the broader resonance from the Na sites of the electrode more clearly.

studies as defects and also when they were intentionally introduced by using different O/F ratios in the starting

materials.<sup>15,24,25</sup> Note that this disorder may also introduce additional disorder in the two Na sublattices. When the pristine samples are heated at high temperatures in air, these minor peaks grow in intensity (see Supplementary Figure S3b).

As in the analysis of the XRD patterns, the series of  $^{23}\text{Na}$  spectra reveal at least three distinct stages (I, II, III) (Figure 4a). At the beginning of Stage I, the minor resonances below 50 ppm disappear quickly. The intensities of both the Na1 and Na2 resonances decrease simultaneously, their linewidths becoming noticeably broader after  $x = 0.3$ . The latter is ascribed to the onset of  $\text{Na}^+$  mobility enabled by the extraction of Na and the creation of Na vacancies. Only small shifts in peak positions are observed at early Stage I, consistent with the relatively small lattice parameter changes seen in XRD. However, the Na extraction is accompanied by vanadium oxidation, which is expected to result in an overall shift of the  $^{23}\text{Na}$  resonances, most likely to lower frequencies since the number of unpaired electrons decreases on charge. Thus the results in early Stage I are counterintuitive and suggest that the V unpaired electrons are localized at this stage, i.e., the residual Na ions are not affected by the change in oxidation state of vanadium ions beyond their local environment. Furthermore, the results suggest that electrons are removed on Na extraction from orbitals that are not directly involved in the transfer of spin-density from vanadium to the Na s orbitals.

The occupancy of the two Na sites can be monitored during Stage I by quantifying the peak area of the Na1 and Na2 sites (Figure 4b). The total measured Na content by NMR vs the extracted Na ( $x$ ) measured electrochemically decreases linearly with a slope of  $-1$  (Figure 4b), which confirms that the NMR analysis is quantitative. Furthermore, the rate of Na1 extraction is twice that of Na2 in Stage I. Considering that the occupancy ratio of Na1:Na2 is 2:1, the results indicate that there is no noticeable preference for Na2 over Na1 removal in Stage I, consistent with the XRD refinement results (Supplementary Information), but in contradiction to the earlier hypothesis that Na2 is preferentially removed first and that Na2 is less stable than Na1.<sup>14,16</sup>

As more Na is extracted, the two  $^{23}\text{Na}$  resonances move closer to each other and coalesce when a total of 0.9 Na is removed from the structure. A single, broad resonance is now observed at approximately 130 ppm, with a shoulder to lower frequencies. The peak maximum of the resonance, 130 ppm, observed for the  $x = 0.9$  sample is close to the average shift of the Na1 and Na2 sites (129 ppm) of pristine  $\text{Na}_3\text{V}_2(\text{PO}_4)_2\text{F}_3$ , weighted according to their site occupancies. Coalescence is ascribed to the larger amplitude/faster motion of both the Na1 and Na2 ions, eventually leading to complete coalescence of the two  $^{23}\text{Na}$  resonances. On the basis of the separation in frequency between the Na1 and Na2 resonances,  $\Delta$  (i.e., 9.3 kHz), coalescence indicates that the frequency of Na1–Na2 exchange,  $k_{\text{ex}}$ , occurs with a frequency equal or greater than<sup>26</sup>

$$k_{\text{ex}} = \Delta/2$$

$$\text{i.e., } k_{\text{ex}} = 4.6 \text{ kHz} \quad (2)$$

A noticeable reduction in shift of more than 28 ppm is then seen between  $x = 0.9$  and 1.0. The possible origins of this are discussed later. Variable-temperature  $^{23}\text{Na}$  NMR measurements of the cycled electrode  $\text{Na}_{3-x}\text{V}_2(\text{PO}_4)_2\text{F}_3$  at  $x = 1.0$  (Figure 4c) confirm that the single resonance observed at this stage originates from the motion-induced coalescence of (at least) two  $^{23}\text{Na}$  resonances: at 253 K, Na motion is sufficiently

reduced so that the frequency of Na hops between the Na1 and Na2 sites is now slower than the separation of the two  $^{23}\text{Na}$  resonances (in frequency units), and two distinct  $^{23}\text{Na}$  peaks (from Na1 and Na2) can then be resolved. (A peak at approximately 50 ppm is also observed, which is reminiscent of the original defect resonance at 50 ppm and is thus assigned to Na nearby  $\text{V}^{4+}$  either created by Na removal or present initially due to O/F defects. The reappearance of this resonance at low temperatures indicates that the Na environments that give rise to this resonance are in the same phase as the sites that give rise to the Na1 and Na2 resonances).

In Stage II, the single  $^{23}\text{Na}$  resonance steadily shifts toward 0 ppm while also decreasing in intensity, a sign of a single-phase Na extraction process. At the beginning of Stage III ( $x = 1.5$ ), a new peak emerges (87 ppm) and dominates quickly. The new resonance continuously shifts to lower frequencies until the end of charge with a faster rate as compared with that in Stage II. No new phase is evident from the diffraction, and thus this change involves local structural changes and/or is electronic in nature.

The static  $^{23}\text{Na}$  spectrum (Figure 4d) of the pristine  $\text{Na}_3\text{V}_2(\text{PO}_4)_2\text{F}_3$  electrode ( $x = 0$ ), acquired at the beginning of an *in situ* NMR experiment, shows a broad resonance at approximately 160 ppm, spreading from 0 to 400 ppm, from the superposition of the resonances from both the Na1 and Na2 sites, in addition to a sharp resonance at  $<0$  ppm from the electrolyte. The broad resonance exhibits only a very small shift to lower frequencies at the beginning of Stage I. Significant line broadening results in an apparent reduction in the peak intensity after  $x = 0.6$ , and the resonance is barely visible at the end of Stage I ( $x = 0.6$ –1.0) and in Stage II ( $x = 1.0$ –1.4). A narrower resonance centered around 70 ppm appears in Stage III and then again shifts slightly to lower frequencies.

**$^{23}\text{Na}$  Dynamics.** The  $^{23}\text{Na}$  spin-lattice relaxation time  $T_1$  and spin-spin relaxation time  $T_2$  were measured at different states of charge (Figure 5). The dominant mechanism for  $^{23}\text{Na}$   $T_1$

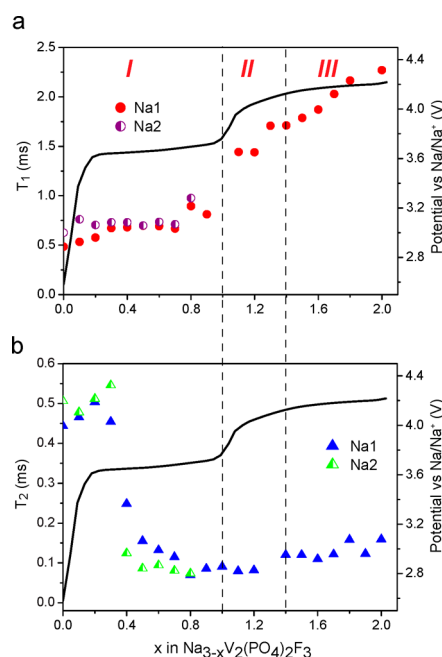


**Figure 5.** Composition dependence of the  $^{23}\text{Na}$  (a)  $T_1$  and (b)  $T_2$  relaxation times of  $\text{Na}_{3-x}\text{V}_2(\text{PO}_4)_2\text{F}_3$  (Na1 and Na2 sites) at different states of charge.

relaxation is the hyperfine interaction between the  $^{23}\text{Na}$  nucleus and unpaired electrons. Other mechanisms include the electric quadrupole relaxation, dipole-dipole, chemical shift anisotropy, and spin-rotation induced relaxation. At the beginning of charge, the  $^{23}\text{Na}$   $T_1$  time is predominantly influenced by the hyperfine interaction, the shorter  $T_1$  of the Na1 site reflecting its larger shift. The gradual merging of the Na1 and Na2  $T_1$  values is ascribed to the onset of Na mobility, which for Na1–Na2 motion on the time scale of the reciprocal of the  $T_1$  time (1–2 kHz) will equalize the  $T_1$  values. A more pronounced increase occurs after  $x = 0.7$ , which coincides with the Na1/Na2 coalescence and shift of the Na resonance, as observed in the 1D  $^{23}\text{Na}$  NMR. The more dramatic increase in  $^{23}\text{Na}$   $T_1$  around  $x = 1.0$  correlates with the sudden change in  $^{23}\text{Na}$  shift (Figure 4a) and the subsequent voltage jump in the electrochemical profile. In Stages II and III, the growth of  $^{23}\text{Na}$   $T_1$  value again tracks the decrease of the  $^{23}\text{Na}$  hyperfine shift.

The  $^{23}\text{Na}$   $T_2$  relaxation time is affected by both the hyperfine interaction and the Na hopping motion. At the beginning of Stage I (from  $x = 0$  to 0.3), with limited Na motion, the hyperfine interaction is the dominant relaxation mechanism: the  $^{23}\text{Na}$   $T_2$  values are very similar to the  $T_1$  values and largely follow the same pattern of change. A dramatic decrease in the  $T_2$  is observed after  $x = 0.3$ , which we ascribed to the onset of more rapid Na motion. Both Na1 and Na2 are affected, suggesting that both ions are involved in the motional process, even at this stage, which is consistent with the coalescence of the resonances from both of these sites after  $x = 0.7$ . The  $T_2$  increases slightly in Stages II and III, which likely results from a combination of the hyperfine interaction and (in Stage III), the reduced Na motion.

Our results should be contrasted with recent  $^{23}\text{Na}$  NMR spectra from a series of  $\text{Na}_3\text{V}_2(\text{PO}_4)_2\text{F}_{3-2\delta}\text{O}_{2\delta}$  derivatives of Park et al.<sup>27</sup> A single resonance at 136 ppm dominates the spectrum of the material with the same nominal composition as that studied here. A weak unassigned resonance is seen at approximately 100 ppm. We suggest that these authors are observing the effect of the onset of Na motion in their spectra, perhaps due to slight differences in stoichiometry and/or the fact that their spectra were acquired at a lower magnetic field strength (9.4 T). (Coalescence between the Na1 and Na2 resonances will occur at a lower frequency of  $\approx 2.6$  kHz at 9.4 T). A single resonance is seen at 71 ppm for  $\text{Na}_3\text{V}_2(\text{PO}_4)_2\text{FO}_2$ , the sample containing only  $\text{V}^{4+}$ . This spectrum is consistent with our assignment of the general shift of the  $^{23}\text{Na}$  resonance to lower frequencies as being due to the oxidation of  $\text{V}^{3+}$  to  $\text{V}^{4+}$ .

**$^{31}\text{P}$  NMR.** The  $^{31}\text{P}$  NMR spectra from the same samples analyzed by  $^{23}\text{Na}$  NMR are shown in Figure 6a. Two dominant, more intense resonances are observed at 6096 and 4600 ppm in the as-synthesized material in addition to a series of weaker resonances at lower frequencies, indicating the presence of a variety of  $^{31}\text{P}$  local environments. The crystal structure of  $\text{Na}_3\text{V}_2(\text{PO}_4)_2\text{F}_3$  contains only two different  $^{31}\text{P}$  environments (Figure 1b), denoted as P1 and P2 here. Both P1 and P2 are surrounded by 8 nearest Na neighbors and share corners with four  $\text{VO}_4\text{F}_2$  polyhedra (Figure 1). On the basis of the structural refinement from the neutron diffraction data,<sup>16</sup> P1 sits in a more symmetric environment as compared to P2. P1 is connected to all four V in its first coordination shell with the same V–P1 distance (3.25 Å) and P1–O–V angle ( $137.2^\circ$ ), while P2 has two sets of slightly different V–P2 distances (3.33 and 3.18 Å) and two sets of P2–O–V bond angles ( $131.4^\circ$  and

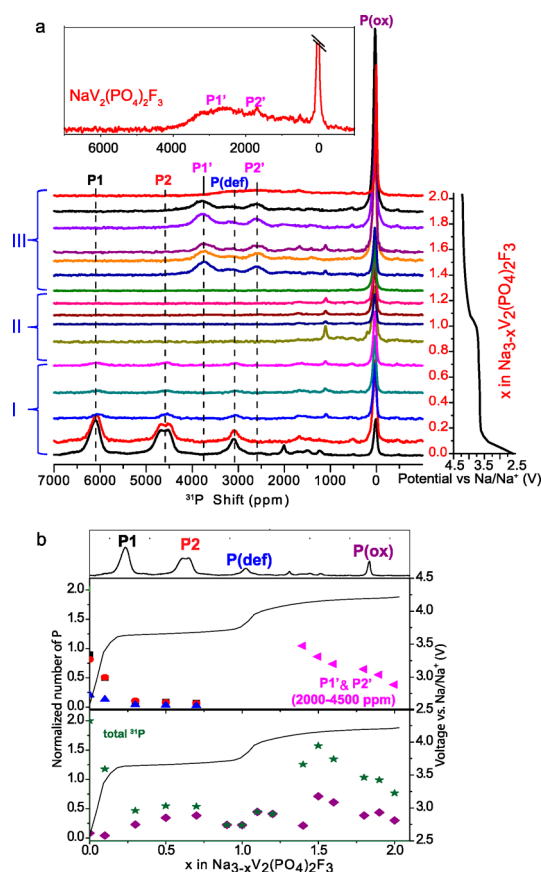


**Figure 6.** (a)  $^{31}\text{P}$  MAS NMR spectra of  $\text{Na}_3\text{V}_2(\text{PO}_4)_2\text{F}_3$  at different states of charge. The isotropic resonances are labeled according to the assignments discussed in the main text. The inset shows the  $^{31}\text{P}$  spectrum of the sample at the end of charge (nominal composition:  $\text{NaV}_2(\text{PO}_4)_2\text{F}_3$ ) with the spectral region above 0 ppm amplified to show the broad P1' and P2' resonances. The spectra were obtained by a stepwise mapping method (4 steps in total). (b) Signal intensity evolution of different  $^{31}\text{P}$  sites following charging: P1 (black filled squares), P2 (red filled circles), P(def) (blue triangles), P(ox) (purple diamonds), the total P1' and P2' intensity (pink triangles), and total P intensity (green stars). The  $T_2$ -corrected  $^{31}\text{P}$  intensities are plotted, where the extracted integrals of all resonances are corrected with a factor of  $1/\exp(-2\tau/T_2)$ , where  $\tau$  is the echo delay before signal acquisition and  $T_2$  is the measured relaxation times of individual peaks (as listed in Supplementary Table S2). Error bars (arising from the integrations) are smaller than the size of symbols. This analysis is associated with a larger error in Stage III due to the difficulty of measuring the  $T_2$  values of the broad overlapping resonances.

$130.8^\circ$ ). Furthermore, P1 is connected to four identical O (O1) atoms, (with V–O1 bond lengths of 1.99 Å), while P2 links to two O (O2) atoms with a V–O2 bond length of 2.05 Å and two O (O3) atoms with a V–O3 bond length of 1.96 Å, resulting in a slightly longer average V–O2/3 distance of 2.00 Å. On the basis of the slightly shorter average V–O bond distance and hence a likely increase in spin-density transfer, we ascribe the resonance at 6096 ppm to P1 and the split resonance centered at 4600 ppm to P2 (Figure 6).

The splitting of the P2 resonance to form a doublet is ascribed to the partial occupancy of the Na2 sublattice (Supplementary Figure S2), the  $\text{P}_2\text{O}_4$  tetrahedron being surrounded by four 50% occupied Na2 sites in its first coordination shell (at 3.18 Å) and four more distant Na1 sites at 3.50 Å, while the  $\text{P}_1\text{O}_4$  tetrahedron is nearby four fully



occupied Na1 sites (at 3.47 Å) and four partially occupied Na2 sites at 4.10 Å.<sup>16</sup> The doublet structure implies local ordering, around the phosphate anions (since more local environments would be expected for random Na2 occupancy). Of the four nearby Na2 sites, not all of the sites can be simultaneously occupied due to the short Na–Na distances (1.87 Å) in these split positions. Only two configurations are possible (Supplementary Figure S2), suggesting that this is the source of the P2 doublet. Typically, <sup>31</sup>P shifts for P near V<sup>3+</sup>, V<sup>4+</sup>, and (diamagnetic) V<sup>5+</sup> are >4000 ppm, 1500–4000 ppm, and close to 0 ppm, respectively,<sup>17</sup> consistent with the assignments of the higher frequency resonances to framework sites nearby V<sup>3+</sup>.

The resonances at around 3100, 2000, and 1200 ppm (denoted as P(def) in the spectra) are ascribed to minor defects in the framework associated with vanadium mixed valency and phosphate groups nearby vanadium with an average valence state larger than V<sup>3+</sup>. The presence of V<sup>4+</sup> in these materials has been suggested previously and may be due to O for F substitution.<sup>15</sup> The concentration of these defect resonances is not significantly affected when the pristine Na<sub>3</sub>V<sub>2</sub>(PO<sub>4</sub>)<sub>2</sub>F<sub>3</sub> material is heated at temperatures of up to 400 °C (Supplementary Table S1b, Figure S3). In contrast, the peak at 0 ppm (denoted as P(ox)) grows noticeably on heating and is ascribed to the highly oxidized impurities, most likely at the surfaces of the particles. (Note that Park et al. have also observed resonances at –60 to +60 ppm, in their study of the related NASICON-phases Na<sub>1.5</sub>V(PO<sub>4</sub>)<sub>1</sub>F<sub>0.5</sub>O and Na<sub>1.5</sub>V(PO<sub>4</sub>)F<sub>0.7</sub>O<sub>0.8</sub>.<sup>25</sup> This observation of resonances at much lower frequencies may be a consequence of the higher (average) oxidation state of these materials (V<sup>3.8+</sup> and V<sup>4+</sup>, respectively); it is also possible that resonances at higher frequencies could not be detected because of the severe challenge associated with the acquisition of spectra from materials with mixed V<sup>4+</sup>/V<sup>3+</sup> oxidation states (see below) and possibly the limited spectral range investigated in this study).<sup>25</sup>

The evolution of the <sup>31</sup>P spectra on charge reveals significant changes in the <sup>31</sup>P local environments (Figure 6). In Stage I, as Na is extracted, the P1 and P2 peaks rapidly decrease in intensity until  $x = 0.3$ . The residual weak peaks almost completely vanish at the end of Stage I ( $x = 1.0$ ). The plot quantifying the intensity of the <sup>31</sup>P spectra (Figure 6b) shows that the rate of signal loss from P1 + P2 is approximately 4 times larger than the rate of Na extraction (and loss of <sup>23</sup>Na intensity). Structurally, four PO<sub>4</sub> ions (2\*P1 and 2\*P2) are located in the first coordination shell of each Na ion. Similarly, each phosphate ion is surrounded by four vanadium ions. Thus the removal of one Na ion and the associated oxidation of one V<sup>3+</sup> ion to V<sup>4+</sup>, assuming localization of the electron hole on one vanadium ion, will affect four nearby phosphate groups. The reduction in the intensity of P1 and P2 does not lead to any observable new resonances at this stage. The intensity of the peaks between 0 and 4000 ppm also decreases, similar to the P1 and P2 resonances, suggesting that the defect sites are in the same phase as P1 and P2. In contrast, the peak at 0 ppm grows in intensity.

In Stage II, no distinct peaks are observed in the <sup>31</sup>P spectra, except the 0 ppm peak and the minor peaks with shifts of less than 2000 ppm. A slight increase in the peak intensity at 0 ppm is again observed. In Stage III, two distinct intense peaks suddenly appear at 3749 and 2605 ppm, denoted as P1' and P2', which we ascribe to the P1 and P2 sites in the new structure formed at the beginning of Stage III. The P(def)

resonance also reappears providing further evidence that this defect resonance is within the same phase that gives rise to the P1/P2 and P1'/P2' resonances.

The positions of the P1' and P2' resonances remain approximately the same in Stage III until  $x = 2.0$ , but there is a gradual intensity loss, which is most likely associated with an increased line width of the resonances arising from a distribution of paramagnetic shifts, due to further Na extraction. This is clearly illustrated by the spectrum seen at  $x = 2.0$ , where a very broad resonance spanning from 4000 to 0 ppm is observed.

## DISCUSSION

On the basis of the electrochemical profile, XRD, and NMR spectroscopy, the evolution of the structural and dynamical changes induced by Na extraction from the Na<sub>3</sub>V<sub>2</sub>(PO<sub>4</sub>)<sub>2</sub>F<sub>3</sub> electrode battery charging proceeds as follows:

**Stage I.** From  $x = 0$  to 0.6, Na1 and Na2 are removed in a ratio consistent with their relative occupancy in the structure (*ex situ* <sup>23</sup>Na NMR), suggesting little site preference for Na removal at this stage. This is in contrast to earlier reports, which have suggested that Na2 is less stable and removed first from the structure.<sup>15,16</sup> Na at defect sites (with <sup>23</sup>Na shifts <50 ppm) is also removed at this early stage. The Na cation removal is associated with a gradual increase in *c*-parameter, largely due to increased electrostatic repulsions between F–F and O–O anions near the Na ions that are removed.<sup>16</sup> Unfortunately, the quality of the XRD data of the charged samples was not sufficient to obtain reliable O/F positions so as to further explore this suggestion. Synchrotron XRD studies are currently in progress to obtain further information. The <sup>31</sup>P resonance shows a dramatic decrease in intensity in this stage (Figure 6), this observation indicating that phosphate ions nearby the V<sup>4+</sup> ions created by Na extraction are not observable under the experimental conditions used in this study. The <sup>31</sup>P intensity drops at a rate that is 4 times larger than the rate of V<sup>3+</sup> to V<sup>4+</sup> oxidation, correlating with the number of V ions in the local phosphate coordinate shell (four). This strongly implies that the electron holes (that create V<sup>4+</sup>) are at least partially localized (on the NMR time scale) since a smoother progression of <sup>31</sup>P shifts and/or a different rate of loss of <sup>31</sup>P intensity might be expected for a completely delocalized system. The onset of slow Na mobility occurs during this stage, as indicated by a pronounced decrease in *T*<sub>2</sub> between  $x = 0.3$  and 0.4 and the equalization of the *T*<sub>1</sub> values for the two Na sites at this point (Figures 4 and 5). The mobility is not sufficient in early Stage I, however, to cause signal coalescence. The loss of <sup>31</sup>P signal during this stage most likely arises from the distribution of hyperfine shifts caused by the distribution of local environments containing different V<sup>3+</sup>/V<sup>4+</sup> ratios but may also arise from the onset of <sup>23</sup>Na motion, the <sup>31</sup>P spectra being sensitive to the nearby Na ions, and/or the very slow hopping of electrons (holes) between V ions (see below), both effects reducing the <sup>31</sup>P *T*<sub>2</sub> times.

The rate/amplitude of the Na<sup>+</sup> motion increases as more Na is extracted, eventually leading to coalescence of the two distinct Na1 and Na2 sites (in Stage I<sub>b</sub>) when a total of 0.9 Na is removed from the structure, indicating a Na1–Na2 two-site exchange rate of ~4.6 kHz. The behavior in late Stage I ( $x = 0.6$ –1.0) is distinct from that in early stage I ( $x = 0$ –0.6): the potential increases more rapidly, the *a*-parameter drops faster, Na coalescence occurs, the *T*<sub>1</sub> increases more noticeably, and a noticeable jump in <sup>23</sup>Na shift between  $x = 0.9$  and 1.0 occurs.



The more rapid intensity reduction observed in the *in situ*  $^{23}\text{Na}$  spectra at this stage largely results from Na motion-induced line broadening.

Either a significant electronic and/or structural rearrangement must have taken place during or at the end of Stage I, because there is a noticeable step in the potential associated with Na removal in Stage I and II. Earlier work has suggested that the origin of this step lies in the preferential removal of Na from the Na2 sites during Stage I, the Na occupying the lower energy Na1 sites being removed only during stages II and III. We see no evidence for preferential removal of Na from the Na2 sites, at least until  $x = 0.9$ . Thereafter, coalescence prevents further simple analysis of the relative site occupancies, although the peak position of the coalesced resonance suggests that both Na1 and Na2 sites are present. It is tempting to ascribe the noticeable change in Na hyperfine shift between  $x = 0.9$  and 1.0 to a cation rearrangement, but the low temperature  $^{23}\text{Na}$  NMR data acquired for the  $x = 1.0$  sample (Figure 4c) still indicates that two major Na environments are present. Thus we suggest that the cause of the change in hyperfine sites is electronic in origin, a different arrangement of the unpaired electrons within the three  $V t_{2g}$  orbitals resulting in a noticeably smaller shift.

The  $\text{VO}_4\text{F}_2$  octahedron in the as-synthesized material is slightly distorted with axial V–F bonds of 1.88 and 2.08 Å and V–O bonds of  $\sim 2.00$  Å where the four O sit above the nominal  $\text{VO}_4$  plane displaced toward the F atom with the shorter V–F distance away from the bridging F atom (see Supplementary Figure S4). This (approximately) tetragonal distortion will lift the degeneracy of the three  $t_{2g}$  orbitals that contain the two unpaired electrons of the  $d^2 V^{3+}$  ion, which may, depending on the nature and size of the tetragonal distortion, result in unequal occupancies of the  $d_{xy}$  vs the  $d_{xz}/d_{yz}$  orbitals. It is challenging in  $V^{3+}$  and  $V^{4+}$  compounds to predict *a priori* the relative energies of the  $d_{xy}$ ,  $d_{xz}$ , and  $d_{yz}$  orbitals. The more rapid decrease in the  $a$ -parameter in late Stage I ( $x = 0.6$ –1.0) may suggest that the electron is being removed from an orbital in the  $a$ – $b$  plane (the  $d_{xy}$  orbital) during this stage (reducing the electron–O ligand repulsions). If this is the case, then this implies that this orbital has a larger effect on the Na hyperfine shift, presumably because the overlap with this orbital is more effective.

Thus, we tentatively suggest that the structural change during late Stage I ( $x = 0.6$ –1.0) is due to a combination of (or driven by) two factors (which may be intimately connected): the rapid mobility of Na ions between Na1 and Na2 sites, which will help prevent local distortions of the framework due to tightly bound Na ions, and the preferential removal of the electron density from a different orbital during late Stage I (possibly the  $d_{xy}$  orbital) presumably caused by an associated structural distortion of the  $\text{VO}_4\text{F}_2$  that changes the relative energies of the different  $t_{2g}$  orbitals. Localization of the electrons in the  $d_{xz}/d_{yz}$  orbitals provides a mechanism for increased V–O  $\pi$  bonding via the oxygen p orbitals and the empty  $d_{xy}$  orbital (reducing the V–O bond lengths and thus the  $a$  cell parameter). (Less effective  $\pi$  bond formation is expected with the F orbitals.) The suggestion that electrons are removed from the  $d_{xy}$  orbital is also consistent with an increase of the  $c$ -parameter in Stage I, since it involves an increase in average occupancy of the  $d_{xz}/d_{yz}$  orbitals from approximately 2/3 electrons per orbital at  $x = 0$  to 3/4 (i.e., the average of  $d_{xz}^1 d_{yz}^1$  ( $V^{3+}$ ) and  $d_{xz}^0 d_{yz}^1/d_{xz}^1 d_{yz}^0$  ( $V^{4+}$ ) configurations) at  $x = 1.0$ . Furthermore, since the  $d_{xz}/d_{yz}$  orbitals will contain only an average of 1.5 electrons at the end of Stage I, hopping between

the  $d_{xz}/d_{yz}$  orbitals can occur, being mediated via the, albeit weak, interactions with the F 2p orbitals, resulting in a mixed valent F–V( $\text{O}_4$ )FV( $\text{O}_4$ )–F dimer at  $x = 1.0$ . Fast hopping is unlikely to occur during early Stage I on the basis of the change in the  $^{31}\text{P}$  intensity on Na extraction. *Ab initio* calculations are currently in progress to explore some of these proposals and to determine the relative energies of the different orbitals.

**Stage II.** The changes in this stage bear some resemblance to phenomena that occur in Stages I. Extraction of electrons has very little effect on the Na hyperfine shift, suggesting that the electrons are predominantly being removed from the same orbitals as those involved in early Stage I (tentatively  $d_{xz}/d_{yz}$ ). As in Stage II no  $^{31}\text{P}$  signal is observed, suggesting a distribution of local environments and/or short  $T_2$  times perhaps due to Na/electron hopping.

**Stage III.** The most striking observations now are the appearance of the P1' and P2'  $^{31}\text{P}$  signals and a sharper  $^{23}\text{Na}$  resonance in the *in situ*  $^{23}\text{Na}$  NMR spectra at the beginning of Stage III. The average vanadium oxidation state at this point is approximately  $V^{3.75+}$ . We suggest that the electron hopping between the V ions in the dimer no longer occurs in Stage III and discrete  $V^{4+}$  and  $V^{3+}$  ions are present. This appears to correlate with a reduction in Na mobility (as measured by the GITT experiments and in agreement with the  $^{23}\text{Na}$  *in situ* NMR measurements). A splitting of the  $^{23}\text{Na}$  resonances in the *ex situ*  $^{23}\text{Na}$  spectra is also seen at  $x = 1.5$  (Figure 4a), indicating that two different local or averaged environments are present, one containing slightly more  $V^{3+}$ . Further extraction of Na results in an intensity loss of  $^{31}\text{P}$  resonances, reminiscent of the process in early Stage I, and which we ascribe to a broad distribution of hyperfine shifts. The oxidation of vanadium is manifested by the decreasing  $^{23}\text{Na}$  shifts and increasing  $^{23}\text{Na}$  relaxation times (both  $T_1$  and  $T_2$  values) (Figures 4 and 5).

## CONCLUSIONS

The structural and dynamical changes of  $\text{Na}_3\text{V}_2(\text{PO}_4)_2\text{F}_3$  during the charge process when used as a positive electrode in a NIB have been investigated by high-resolution solid-state  $^{23}\text{Na}$  and  $^{31}\text{P}$  NMR, complemented by electrochemical and XRD analyses. The two Na and two P sites can be resolved by NMR, allowing their fate to be monitored as Na is removed. The results reveal a complex process and show that the three different stages of charging (I, II, and III) involve distinct changes in Na and electronic mobility and V electronic configurations. Na extraction involves a loss of Na ions from both the Na1 and Na2 sites, NMR and XRD confirming that this process is nonselective at least until  $x = 0.9$  (based on the NMR). Na mobility increases steadily on charging as more Na vacancies are formed in the structure. At  $x = 0.9$ , coalescence of the Na1 and Na2 resonances is observed, indicating that the hopping frequency between these two sites is  $\geq 4.6$  kHz. This rapid Na motion must in part be responsible for the good electrochemical performance of this material.

A noticeable structural change occurs during late Stage I, which also results in a significant electronic change, as manifested by the sudden change in the Na hyperfine shift. We suggest that this involves a rearrangement of the electrons within the  $V t_{2g}$  orbitals, but calculations are required to explore this further. We tentatively suggest that the preferential removal of electrons from the  $V d_{xy}$  orbital leads to the anisotropic changes in the long-range structure, i.e., the decrease in the  $a(b)$ -parameters and increase in the  $c$ -parameter, although

changes in repulsions between the vanadium octahedra caused by the loss of Na ions and changes in oxidation state may also play a role. The onset of electron hopping between the two V atoms within the  $F-V(O_4)FV(O_4)-F$  dimer likely occurs at this point. The dynamics of both electrons and Na significantly affect the local environments experienced by  $^{31}P$ . The  $^{31}P$  signal disappears initially but reappears at  $x = 1.5$ , the latter being ascribed to a change in the electron-hopping rate. This is correlated with a reduction in Na mobility, and the decrease in Na diffusivity extracted from the GITT measurements.

The study shows how NMR spectroscopy in combination with XRD can be used to probe long- and short-range structure and dynamics and provide insight into the mechanism of Na extraction from  $Na_3V_2(PO_4)_2F_3$  when used in a NIB.

## ■ ASSOCIATED CONTENT

### Supporting Information

Detailed information about the whole set of *in situ* XRD patterns of the cycled electrodes and XRD and NMR of oxidized  $Na_3V_2(PO_4)_2F_3$  pristine materials. This material is available free of charge via the Internet at <http://pubs.acs.org>.

## ■ AUTHOR INFORMATION

### Corresponding Authors

\*E-mail: [yyang@xmu.edu.cn](mailto:yyang@xmu.edu.cn).

\*E-mail: [cpg27@cam.ac.uk](mailto:cpg27@cam.ac.uk).

### Notes

The authors declare no competing financial interest.

## ■ ACKNOWLEDGMENTS

Z.L. acknowledges financial support from the EU ERC Advanced Fellowship to C.P.G. and a State Scholarship Fund from China Scholarship Council (No. 2011631036). Y.Y.H. acknowledges support from a Newton International Fellowship from the Royal Society and a Marie Curie International Incoming Fellowship (PIIF-GA-2011\_299341). M.T.D. acknowledges funding from the Cambridge Commonwealth Trusts and Trinity College, Cambridge. Y.Y. acknowledges funding from National Basic Research Program of China (973 program, Grant No. 2011CB935903) and National Natural Science Foundation of China (Grant No. 21233004).

## ■ REFERENCES

- (1) Armand, M.; Tarascon, J. M. *Nature* **2008**, 451, 652.
- (2) Palomares, V.; Serras, P.; Villaluenga, I.; Hueso, K. B.; Carretero-Gonzalez, J.; Rojo, T. *Energy Environ. Sci.* **2012**, 5, 5884.
- (3) Wenzel, S.; Hara, T.; Janek, J.; Adelhelm, P. *Energy Environ. Sci.* **2011**, 4, 3342.
- (4) Ellis, B. L.; Nazar, L. F. *Curr. Opin. Solid State Mater. Sci.* **2012**, 16, 168.
- (5) Kim, S. W.; Seo, D. H.; Ma, X. H.; Ceder, G.; Kang, K. *Adv. Energy Mater.* **2012**, 2, 710.
- (6) Ong, S. P.; Chevrier, V. L.; Hautier, G.; Jain, A.; Moore, C.; Kim, S.; Ma, X. H.; Ceder, G. *Energy Environ. Sci.* **2011**, 4, 3680.
- (7) Barker, J.; Saidi, M. Y.; Swoyer, J. L. *J. Electrochem. Soc.* **2003**, 150, A1394.
- (8) Le Meins, J. M.; Crosnier-Lopez, M. P.; Hemon-Ribaud, A.; Courbion, G. *J. Solid State Chem.* **1999**, 148, 260.
- (9) Gover, R. K. B.; Burns, P.; Bryan, A.; Saidi, M. Y.; Swoyer, J. L.; Barker, J. *Solid State Ionics* **2006**, 177, 2635.
- (10) Gover, R. K. B.; Bryan, A.; Burns, P.; Barker, J. *Solid State Ionics* **2006**, 177, 1495.
- (11) Barker, J.; Gover, R. K. B.; Burns, P.; Bryan, A. J. *Electrochem. Solid-State Lett.* **2006**, 9, A190.
- (12) Hao, X.; Liu, Z.; Gong, Z.; Wen, W.; Tan, S.; Yang, Y. *Sci. Sin. Chim.* **2011**, 42, 38.
- (13) Jiang, T.; Chen, G.; Li, A.; Wang, C. Z.; Wei, Y. J. *J. Alloys Compd.* **2009**, 478, 604.
- (14) Chihara, K.; Kitajou, A.; Gocheva, I. D.; Okada, S.; Yamaki, J. *Power Sources* **2013**, 227, 80.
- (15) Serras, P.; Palomares, V.; Goni, A.; de Muro, I. G.; Kubiak, P.; Lezama, L.; Rojo, T. *J. Mater. Chem.* **2012**, 22, 22301.
- (16) Shakoar, R. A.; Seo, D. H.; Kim, H.; Park, Y. U.; Kim, J.; Kim, S. W.; Gwon, H.; Lee, S.; Kang, K. *J. Mater. Chem.* **2012**, 22, 20535.
- (17) Sananes, M. T.; Tuel, A. *Solid State Nucl. Magn. Reson.* **1996**, 6, 157.
- (18) Brown, I. D.; Wu, K. K. *Acta Crystallogr. B* **1976**, 32, 1957.
- (19) Key, B.; Bhattacharyya, R.; Morcrette, M.; Seznec, V.; Tarascon, J. M.; Grey, C. P. *J. Am. Chem. Soc.* **2009**, 131, 9239.
- (20) Weppner, W.; Huggins, R. J. *Electrochem. Soc.* **1977**, 124, 1569.
- (21) Larson, A. C.; Von Dreele, R. B. *Los Alamos National Laboratory Report LAUR 86-748*; Los Alamos National Laboratory: Los Alamos, NM, 1994.
- (22) Toby, B. H. *J. Appl. Crystallogr.* **2001**, 34, 210.
- (23) Tong, Y. Y. *J. Magn. Reson., Ser. A* **1996**, 119, 22.
- (24) Serras, P.; Palomares, V.; Goni, A.; Kubiak, P.; Rojo, T. *J. Power Sources* **2013**, 241, 56.
- (25) Park, Y. U.; Seo, D. H.; Kwon, H. S.; Kim, B.; Kim, J.; Kim, H.; Kim, I.; Yoo, H. I.; Kang, K. *J. Am. Chem. Soc.* **2013**, 135, 13870.
- (26) Levitt, M. *Spin Dynamics: Basics of Nuclear Magnetic Resonance*; Wiley: New York, 2008.
- (27) Park, Y. U.; Seo, D. H.; Kim, B.; Hong, K. P.; Kim, H.; Lee, S.; Shakoar, R. A.; Miyasaka, K.; Tarascon, J. M.; Kang, K. *Sci. Rep.* **2012**, 2, 704.